







Long-period directivity pulses of strong ground motion during the 2023 Mw7.8 Kahramanmaraş earthquake

František Čejka ¹, Jiří Zahradník ¹, Fatih Turhan ², Efthimios Sokos³ & František Gallovič ¹

Damages due to large earthquakes are influenced by broadband source effects that remain enigmatic. Here we develop a broadband (0–10 Hz) source model of the disastrous 2023 Mw7.8 Kahramanmaraş, Türkiye, earthquake by modeling recordings of 100 stations. The model combines coherent and incoherent rupture propagation at low and high frequencies, respectively. We adopt a planar 300 km long kinked fault geometry from geology and pre-constrain the slip model from seismic and geodetic data. We demonstrate that the south-westward rupture propagation was delayed by ~15 s and that the observed strong waveform pulses can be explained by the directivity effect due to a specific combination of the coherent and incoherent components. We show that even a rough estimate of major rupture parameters makes the ground motion simulations of such large events possible, and may thus improve the efficiency of rapid, physics-based, shaking estimation for emergency response and seismic hazard assessment.

¹Department of Geophysics, Faculty of Mathematics and Physics, Charles University, Prague, Czech Republic. ²Kandilli Observatory and Earthquake Research Institute (KOERI), Boğaziçi University, Istanbul, Türkiye. ³Department of Geology, Seismological Laboratory, University of Patras, Patras, Greece. email: cejka@karel.troja.mff.cuni.cz

At 01:17 UTC (04:17 Türkiye Time) on February 6, 2023, the broader Türkiye-Syria border region was hit by a destructive Mw7.8 earthquake. It occurred on the East Anatolia Fault (EAF) zone, see Fig. 1. The EAF is a major left-lateral strike-slip contact between the Anatolian microplate and the Arabian plate^{1,2}. This dominant tectonic structure is represented in the Türkiye Seismic Hazard Map (by Disaster and Emergency Management Authority, AFAD). Nevertheless, the human and material losses were enormous, mainly due to collapses of constructions nonconforming with the building code^{3–8}. The event belongs to the largest continental earthquakes experienced in the last ~100 years worldwide, including the 2001 Mw7.8 Kunlun, China, and the 2002 Mw7.9 Denali, Alaska, events. As common for such large shallow earthquakes, the Kahramanmaraş rupture produced meters-long surface displacements along the activated parts of the EAF zone^{6,8,9}.

Early geodetic and seismic data investigations agree on a 300 km long rupture, featuring a large change of the fault strike near longitude 37°E (further referred to as a kink between the major SW and NE fault segments). The epicenter was situated approximately 30 km east of EAF; the earthquake initiated on the Narlı (also Nurdagi Pazarçik) splay fault, oriented NNE, located near the EAF kink, and then the rupture was transferred to EAF, where it propagated bilaterally^{10–15}. The earthquake reactivated segments that ruptured in 1513, 1872, and 1893¹⁶. In the NE segment, the earthquake terminated before reaching the Pütürge segment of EAF, which hosted the 2020 Mw6.8 Elazığ earthquake¹⁶. For the Elazığ earthquake, the dynamic source

inversion of Gallovič et al.¹⁷ revealed a cascading activation of several rupture segments, possibly expected also in the 2023 Kahramanmaraş event. Indeed, Melgar et al.¹⁴ inverted 12 three-component GNSS and 8 three-component strong motion recordings of the 2023 earthquake for rupture propagation on curved faults, revealing variable rupture speed and strongly inhomogeneous slip distribution. Basic characteristics of the slip heterogeneity agree with the InSAR and teleseismic data inversion by Mai et al.¹¹. Rosakis et al.¹⁸, Abdelmeguid et al.¹⁹, and Wang et al.²⁰ resolved supershear stages within the rupture. Moreover, dynamic models by Abdelmeguid et al.¹⁹, Jia et al.²¹, and Wang et al.²⁰ revealed a ~10-s delay of the rupture, back-propagating towards SW from the EAF fault kink. In particular, their dynamic modeling suggests that the initial NE propagation along EAF is necessary (but not sufficient) to trigger delayed nucleation of the SE propagating rupture. The delay of the back-propagating rupture is also indicated in the teleseismic back projections of Okuwaki et al.¹⁵.

So far, all the 2023 Kahramanmaraş earthquake modeling studies have been limited to low-frequency (<1 Hz) seismic data at subsets of available near-fault stations. The recorded peak ground motions generally exceed expectations from empirical models¹¹. Moreover, the observed broadband near-field data feature strong, band-limited long-period pulses, strongly amplifying the velocity waveforms²². These pulse-like motions can cause irreversible structural deformation increasing the collapse risk to high-rise buildings and large-span bridges^{23,24}. Correct modeling of these pulses is not yet fully established, requiring a

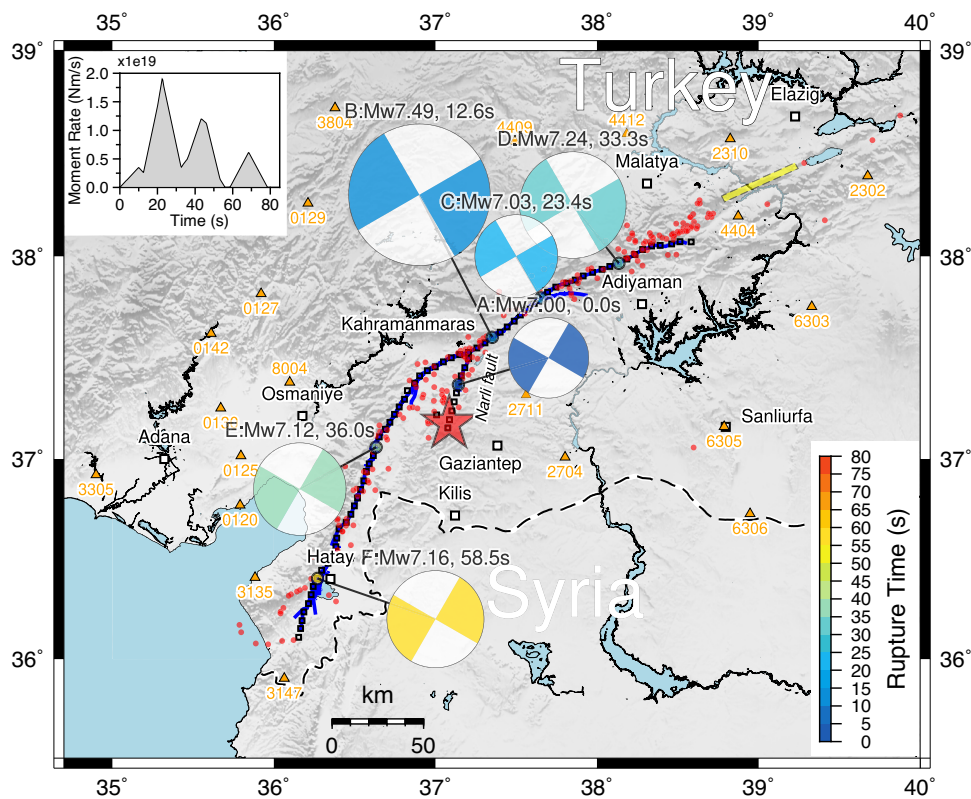


Fig. 1 Multi-point seismic model of the 2023 Mw7.8 Kahramanmaraş, Türkiye earthquake. Space-time moment release is shown by beachballs with radii scaled assuming constant stress drop (i.e., seismic moment to power 1/3) and colored by rupture time relative to the origin time (see the color scale). Focal mechanisms were fixed differently for the SW and NE segments. The major episodes (marked A–F) are detailed in Supplementary Table S1. Star and triangles depict the epicenter and used stations, respectively. The grid of trial sources is shown with small black squares along the faults (blue lines) mapped by Reitman et al.²⁶. Aftershocks located by AFAD are shown as red dots (<https://deprem.afad.gov.tr/event-catalog>). Yellow rectangle depicts the 2020 Mw 6.8 Elazığ earthquake rupture from the dynamic inversion of Gallovič et al.¹⁷. For a stability assessment of this model, see Supplementary Figs. S2–S4. Inset is the moment-rate function of this 6-subevent model.

careful balance between smooth (coherent) and variable (incoherent) rupture propagation at low and high frequencies, respectively.

Here we utilize the complete set of recordings from 100 strong motion instruments within a 150 km fault distance. The data density ranks the earthquake among the best-recorded worldwide. We first determine stable features from fast static slip inversion of GNSS data and multiple point-source inversion of a subset of low-frequency waveforms to constrain large-scale characteristics of the source model. We then supplement the large-scale model with stochastic high-frequency features to simulate the earthquake in a broad frequency range (0.05–10 Hz) and identify rupture processes that fundamentally affect the strong ground motions. The model is validated against observed ground motions in time and spectral domains. Ground motions at a dense set of virtual receivers are calculated to complement the observations by modeling. We also illustrate the sensitivity of the model to individual source features in the Methods section. Finally, we discuss the importance of prior knowledge of the individual source parameters in the ground-motions estimation for rapid emergency response and seismic hazard assessment.

Results

Low-frequency waveforms: multiple point-source inversion.

We select data from 21 strong-motion stations having good azimuthal coverage, being free of instrumental disturbances, and featuring no obvious timing errors¹². We search for multiple point-source (MPS) subevents with the ISOLA software²⁵ using a grid of trial source points designed along mapped fault ruptures²⁶. The MPS model parameters are centroid positions, times, moments, and possibly also focal mechanisms of major subevents, subsequently retrieved from observed waveforms by iterative deconvolution;²⁷ see Methods.

The MPS model can quickly reveal the possibly space-time-separated episodes (asperities) of complex segmented earthquakes. Due to the low-parametric character of the MPS model, the inversion is highly flexible, thus enabling fast examination of hundreds of scenarios from which robust solution characteristics can be identified. A disadvantage is that although the subevent moment is retrieved, slip cannot be estimated until independent information about the subevent spatial size (length, area) is available from further modeling.

Varying trial source positions, frequency ranges, and station subsets produce slightly variable results (see Methods and Supplementary Figs. S1–S4). The stable model features across these variations are summarized in the 6-subevent model in Fig. 1 and Supplementary Table S1: The moment release started on the Narlı splay fault with a relatively weak episode (A) near the origin time. The largest moment release (B) occurred on the NE segment of EAF, spatially centered at ~10 km from the junction of the Narlı fault with EAF, starting 12.6 s after the origin time and being followed by a smaller subevent C (~45 km, 23.4 s). The other major episodes (D, E) occurred almost simultaneously in the NE and SW branches (starting 33.3 s and 36.0 s after the origin, centered at ~90 and ~80 km from the junction, respectively). They thus represent a bilateral rupture with a delay towards SW. The rupture terminated after a major late moment release in SW (F, at ~150 km from the junction, starting at 58.5 s). The position and timing are best resolved for the major episodes B and D (see Methods and jackknife test in Supplementary Fig. S2). The moment-rate function of the 6-subevent model has three major peaks (see inset of Fig. 1).

GNSS static displacements: kinematic slip inversion. For the static slip inversion using the LinSlipInv code²⁸, see Methods, we

use published GNSS static horizontal coseismic displacements¹⁶ (Fig. 2a). Five stations recorded offsets larger than 10 cm in the N or E components. We approximate the fault by a 300 km long planar rupture, with a kink in its middle, i.e., two major planar fault branches. We neglect the initial splay fault rupture. We assume a vertical fault of a 20 km width corresponding to the regional seismogenic width²⁹.

The inversion is stabilized by spatial smoothing and positivity constraints (see Methods). The optimal smoothing is found by a grid search based on the resulting data misfit and inferred seismic moment. The data fit and slip distribution for the preferred model are shown in Fig. 2a, b, respectively. As discussed in Methods, the depth resolution of the GNSS inversion is poor (due to the vertical fault geometry and surface measurements), while the lateral resolution is ~50 km. Nevertheless, the slip model suggests a patch-like (segmented) moment release, as also indicated by the multiple point-source MPS model explained above.

Comparing the GNSS and MPS seismic model, we can assign timing to the slip patches in Fig. 2; see also Supplementary Table S1: Geodetic patches A + B on the NE segment are linked with the 1st and 2nd MPS episodes starting at 0 and 12 s, C and D are related with the 3rd and 4th seismic episodes starting at 23 and 33 s, respectively. Subsources E and F are linked with the 5th and 6th seismic moment release that occurred 36 and 59 s, respectively, on the SW segment.

The models agree in basic characteristics with other published source models. For example, our position of major asperities on the NE segments B and D agrees with Goldberg et al.¹⁰, Melgar et al.¹⁴, and Mai et al.¹¹. Our patches on the SW segment are an analogy of the Goldberg et al.¹⁰ model and the geodetic slip inversion result of Mai et al.¹¹. Note that the SW segment is the place of the largest difference between the geodetic and teleseismic models of Mai et al.¹¹. Our moment-rate function agrees well with Goldberg et al.¹⁰, Melgar et al.¹⁴, Okuwaki et al.¹⁵, and Jia et al.²¹ up to ~55 s. This corresponds to the space-time robustness of our subevents B and D. At later times, affected mainly by the SW segment, the time functions differ among studies, our being relatively close to Jia et al.²¹.

Modeling of broadband ground motions. To model strong ground motions in a broad frequency range (0.05–10 Hz), we utilize the kinematic Hybrid Integral-Composite (HIC) approach³⁰; see also Methods for all details. The model represents the rupture process by randomly distributed overlapping rectangular subsources with fractal number-size distribution. The hybrid approach combines coherent wavefield contribution from the rupture propagation over the subsources at low frequencies and incoherent contribution from the subsources treated as point sources at high frequencies. In addition, the point sources are considered to feature random variations of the focal mechanism to weaken the radiation pattern at high frequencies to a realistic level. The wavefields are crossover-combined in a frequency range of 0.1–0.4 Hz for stations within 10 km from the fault and 0.05–0.2 Hz elsewhere. The hybrid combination of the two modeling approaches simulates the directivity effect that weakens with increasing frequency (see Methods for tests demonstrating the adequacy of the crossover bands). We assume a constant rupture velocity for simplicity. We utilize synthetic Green's functions in the entire frequency range, considering a 1D regional velocity model by Acael et al.³¹ with added shallow low-velocity layers to account for high-frequency amplification of a generic rock site; see Methods and Supplementary Fig. S6 for results with the original velocity model of Acael et al.³¹.

The seismic and GNSS data inversions indicate an uneven (“patchy” or asperity-like) structure of the rupture and a time

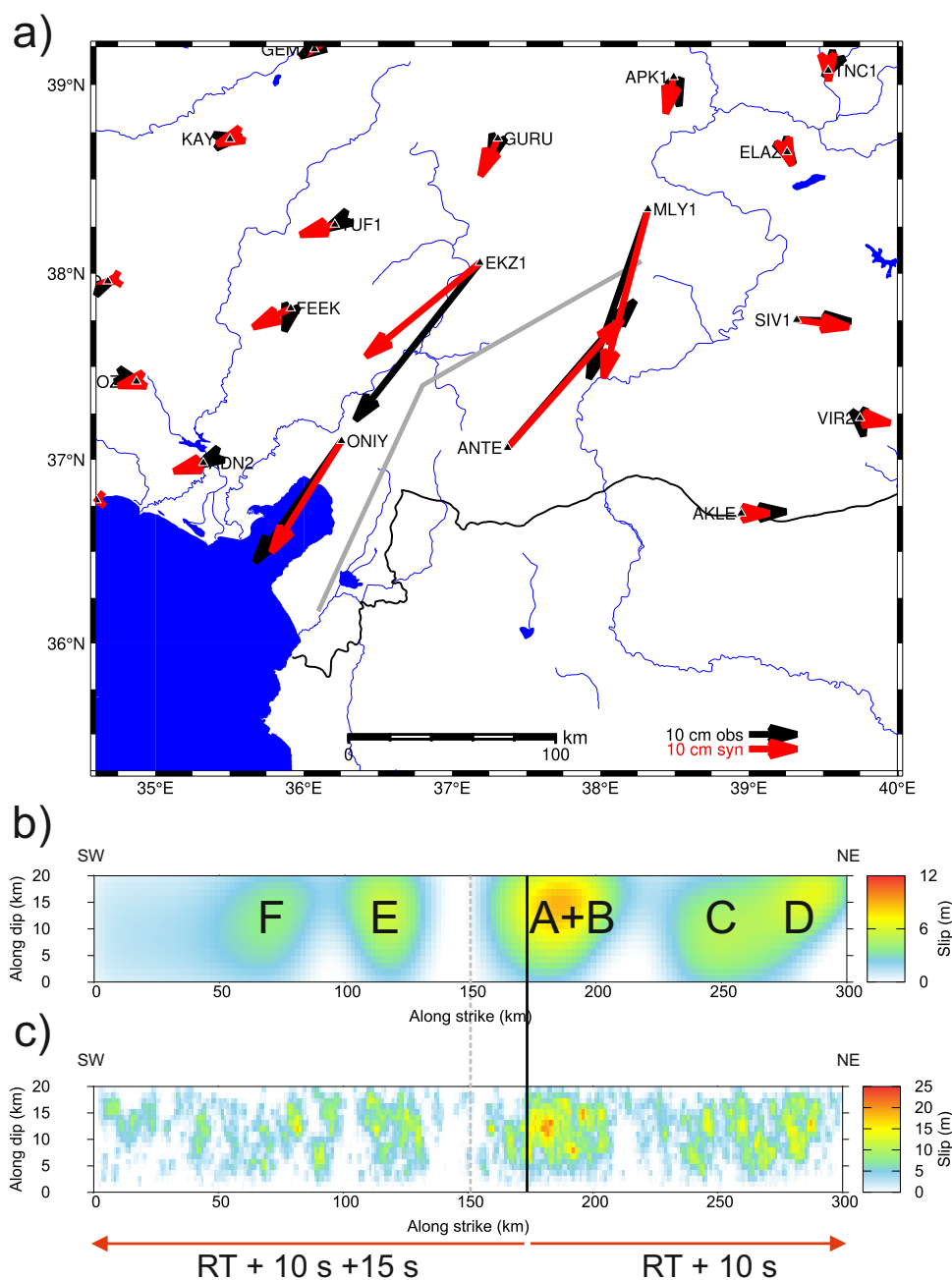


Fig. 2 Static slip inversion of the observed GNSS data of the 2023 Mw7.8 Kahramanmaraş, Türkiye, earthquake and slip model for the broadband ground-motion modeling. **a** Fit of GNSS horizontal displacements from the slip inversion. Gray line shows the trace of the assumed vertical fault. **b** Preferred slip model from the GNSS inversion. The approximate assignment to the MPS subsources of Fig. 1 is labeled A-F. Vertical solid line denotes the intersection with the splay fault (excluded from our modeling). Dashed line marks the fault kink (see panel **a**). **c** Slip distribution obtained by summing slip contributions from all subsources in the HIC model. The subsources are placed randomly following the probability density function obtained by normalizing the slip distribution in panel **b** to unit integral (see Methods for more details). The main features of the rupture kinematics are schematically shown by the red arrows at the bottom (bilateral rupture propagation at constant velocity from the splay fault intersection with depicted rupture delay added to rupture time RT).

delay of the subevents on the SW fault branch. We use the same 300 km long, kinked fault geometry in the broadband modeling as in the GNSS inversion. We do not simulate the initial rupture propagation along the Narlı fault to keep the broadband model simple. Instead, we assume that the rupture formally starts at the intersection of EAF with the Narlı fault, and shift the synthetics on both the NE and SW segments by 10 s (Fig. 2c). No additional station-specific time shifts are applied. We constrain the random spatial distribution of the subsources (independently of their size) by the slip distribution from the GNSS inversion (see Methods).

The subsources then concentrate in the asperity areas, as can be seen from Fig. 2c, which displays a realization of the slip distribution obtained by summing contributions of the subsources. The slip distribution is considered in the low-frequency (integral) part of the simulations, while the same subsources are consistently used in the high-frequency (composite) modeling.

Having prescribed the layout of the subsources, we perform trial-and-error calculations to constrain the remaining rupture parameters (rupture velocity v_p and stress parameter $\Delta\sigma$). In addition, we also search for the delay of the SW segment from the

splay fault intersection (see illustration in Fig. 2c). We determine plausible values by comparing the synthetics in the time domain and the response spectra with observations. We quantify the data fit for all 100 available stations using the modeling bias of spectral accelerations (SA) following the standard approach of Pitarka et al.³². We evaluate SA residuals $r_j(T_i)$ at each station's component j between synthetics M_j and recordings O_j at period T_i ,

$$r_j(T_i) = \ln M_j(T_i) / (O_j(T_i)) \quad (1)$$

The preferred model has values of $v_r = 3.0$ km/s, $\Delta\sigma = 13$ MPa, and a 15-s delay of the SW portion of the rupture propagation (Fig. 2c). The Methods section includes sensitivity tests demonstrating the deteriorating effect on the data fit when changing rupture velocity (Test I) and rupture delay (Test II). Changing the slip distribution (Test III) suggests this effect is only important to the near-fault region.

Figure 3a compares velocity synthetics with recordings at a subset of 9 stations from around the fault (Fig. 4a) to demonstrate the strong spatial variability of the ground motions (see also Supplementary Fig. S7 for all 100 stations). The synthetics explain the overall maximum amplitudes and durations quite well. The preferred model explains the timing, width, and amplitudes of strong velocity pulses dominating the recordings close to the fault (2712, 3137) and in the strike directions of the fault (stations 4404 and 3147), due to the pronounced directivity effect³³. Nevertheless, the sensitivity test in Methods confirms that the directivity effect is band-limited likely due to a decoherence of the rupture propagation at small scales. Note that the slightly later arrival of the main pulse at 3137 suggests local variations in rupture velocity that are not targeted by the modeling. We also point out that the planar fault is a simplification, and thus some of the closest stations might be on the other side of the real geometrically complex fault.

Figure 3b shows the SA modeling bias r_j (gray curves) and its mean and variability evaluated for each component as the average and standard deviation at each period (red solid and dashed curves, respectively). Figure 3b documents an almost zero mean bias at horizontal components and periods. The bias at the vertical components is slightly negative, especially at longer periods. This underestimation of the observation is likely due to the constant (vertical strike-slip) mechanism considered in the modeling, while real data might be affected by (so far poorly resolved) variations of the rupture geometry, including the potential activation of several splay faults. Overall, the modeling results are satisfactory, considering they were derived under simplifying assumptions, especially regarding the wave propagation effects. Indeed, we use only a 1D velocity model of a generic rock site (see Methods), i.e., we neglect site effects due to specific shallow subsurface layers and do not consider any 3D velocity variations (structures like sedimentary basins). For example, synthetics for coastal lowlands stations 0119 and 0120 located on the western side of the Iskenderun Gulf lack strong later peaks, suggesting particular unmodeled complexity in the wave propagation (see Supplementary Fig. S7).

Besides the real stations, we further calculate synthetics on a uniform grid of 460 virtual receivers surrounding the fault and plot the resulting peak ground velocities (PGV) in Fig. 4a. The peak values are rotationally independent mean values (GMRotD50³⁴). Comparison with the real data (color triangles) suggests an overall good fit. The spatial variability of the observations in places with more seismic stations (e.g., near the SW termination of EAF) suggests localized amplification due to site effects.

To reveal possible distance and azimuthal dependencies, Fig. 4b shows a comparison of the observed and synthetic PGV, peak ground displacements (PGD) and accelerations (PGA), all GMRotD50, as a function of station azimuth (measured from the north) and Joyner-Boore fault distance. Both observed and synthetic PGD and PGV (and less clearly PGA) exhibit clear azimuthal dependence with maxima in the fault strike directions (azimuths -155° and 60°). This suggests that the radiated ground motions were strongly directive, and the model captures the observed directivity effect well. We point out that the observed weaker azimuthal dependence of PGA than PGV and PGD is explained in the HIC model by the transition from the coherent to incoherent summation, as we also address in Methods. The synthetics also capture the distance dependence of the ground motion peak values. It all suggests that the wave propagation effects, such as scattering from small-scale random 3D velocity perturbations (likely existing in real medium), do not strongly deteriorate the directivity effect with distance.

Discussion

We have modeled source process and ground motions due to the disastrous 2023 Mw7.8 Kahramanmaraş, Türkiye, earthquake. In agreement with other published models, the low-frequency seismic and GNSS data inversions indicate an asperity-like structure of the rupture and a prominent delay of the rupture propagation southwestward from the intersection of EAF with the initiating Narlı splay fault. The main focus of the present paper is on source modeling extended to broadband frequencies of engineering interest.

To model strong ground motions in a broad frequency range (0.05–10 Hz), we have utilized the kinematic Hybrid Integral-Composite (HIC) approach. By comparison with data in time and spectral domains, we have found plausible values of three main model parameters: stress parameter $\Delta\sigma = 13$ MPa controlling the strength of the high-frequency radiation, the 15-s time delay of the SW fault segment, and constant rupture velocity $v_r = 3.0$ km/s (representing a mean over the fault). We point out that we intentionally keep the model relatively simple regarding details of the rupture propagation (e.g., constant rupture velocity) because the HIC technique is considered a strong-motion prediction tool, intended for general applicability expecting only a rough prior knowledge of earthquake scenario details³⁵. The model explains the peak ground motions (PGD, PGV, PGA) well, including their distance dependence and azimuthal variability controlled by the directivity effect. The synthetics explain durations and overall spectral content in terms of small mean bias of the response spectra over 100 stations. Also explained are strong band-limited directivity pulses due to coherent rupture propagation at large scales, which are present not only close to the fault but also at further distances (Fig. 2). The comparison with observations points to the limitations of the model. They are mainly related to using an average model of a rock station, which cannot capture local high-frequency amplifications due to shallow velocity reduction, generally denoted as site effects, or broader 3D structures as sedimentary valleys. Future studies can pinpoint such details of individual stations and incorporate them into the modeling.

The HIC approach combines coherent wavefield contribution from the rupture propagation at low frequencies and incoherent contribution from randomly distributed overlapping subsources with fractal number-size distribution at high frequencies. The hybrid combination of the two modeling approaches simulates the directivity effect that weakens with increasing frequency. As we show in comprehensive numerical tests (see Methods), this type of directivity enables properly explaining the observed

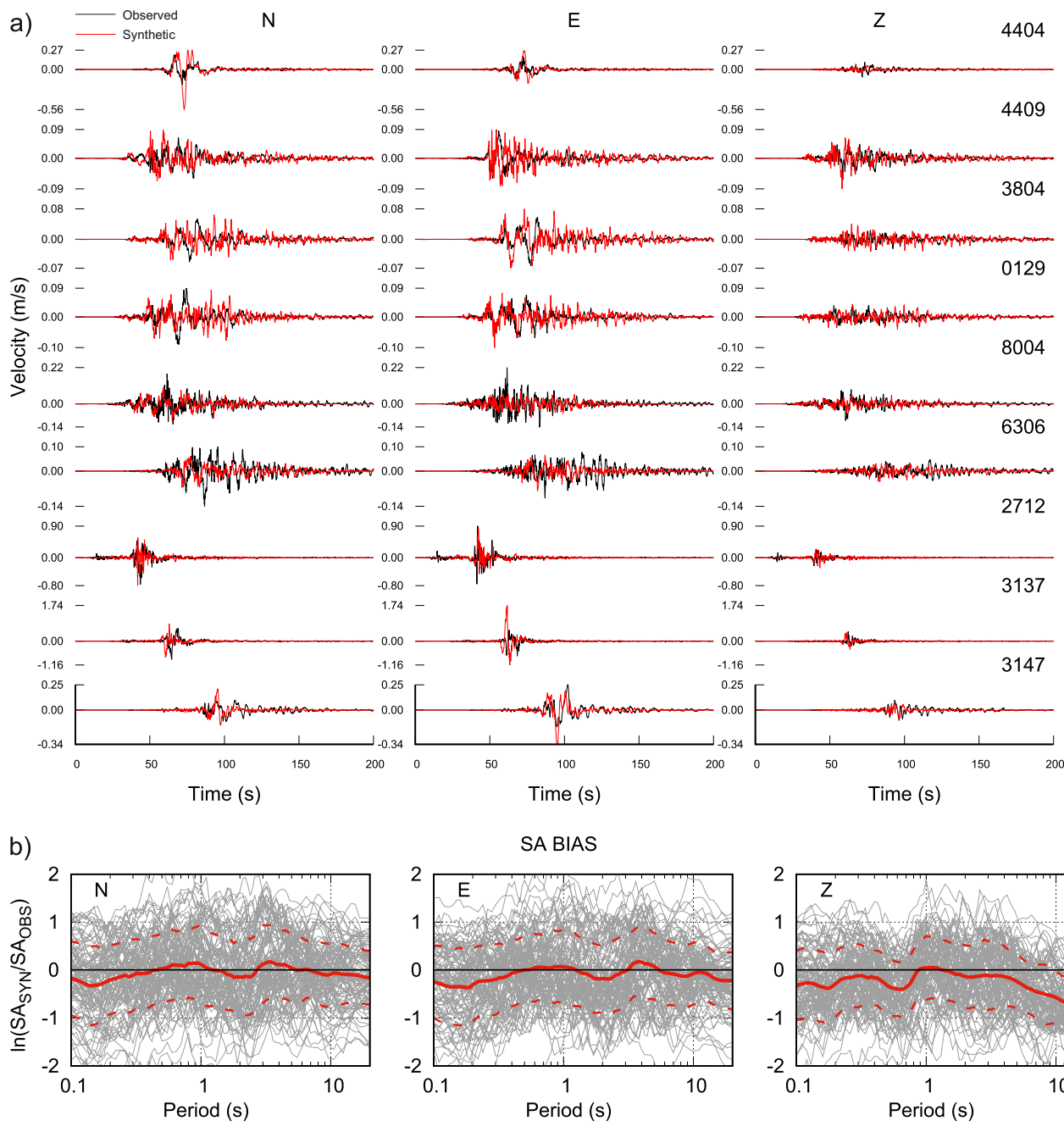


Fig. 3 Modeling result for the preferred broadband source model. a Comparison between synthetic (red) and observed (black) three-component velocity waveforms for selected stations from around the fault (see Fig. 4a). Waveforms start at the origin time. See Supplementary Fig. S7 for all 100 stations. **b** Spectral acceleration (SA) modeling bias (Eq. (1)) plotted for individual components as a function of a period (gray lines). Mean and ± 1 standard deviation over stations are depicted by red solid and dashed lines, respectively.

strength of the directivity velocity pulses and the azimuthal dependence of the peak motions. The latter is stronger for PGD and PGV, while rather weak for PGA (Fig. 4a). Moreover, in the PGV and PGD distance plots, the directivity is seen up to ~ 100 km (Fig. 4b). Contrarily, the tests show that despite considering crossover band at slightly higher frequencies for near-fault stations, the coherency of the radiated wavefield must still be limited to low frequency (see Methods and Fig. 5). It all suggests that limited high-frequency directivity is a source effect, as also observed for small events by Pacor et al.³⁶ and Colavitti et al.³⁷. The possible explanation is due to the substantial complexity of the short-scale rupture propagation that inhibits the high-frequency directivity effect^{38,39}.

Another interesting aspect of the simulations is that although our broadband rupture model does not include coseismic surface slip found in field observations^{8,9}, no prominent wavefield components are missing in the frequency range considered, especially at larger distances from the fault. As Kaneko et al.⁴⁰ demonstrated, neglecting shallow velocity strengthening rheology or very large fracture energy, which would reduce coseismic slip close to the surface, leads to very strong surface waves. Since such waves do not appear in the recordings, the fault slip at the surface likely emerged very slowly, possibly as a very early afterslip (such as documented for the Parkfield earthquake⁴¹), not radiating seismic waves. Therefore, not accounting for surface rupture does not deteriorate the simulations if one is not interested in the fault displacement hazard.

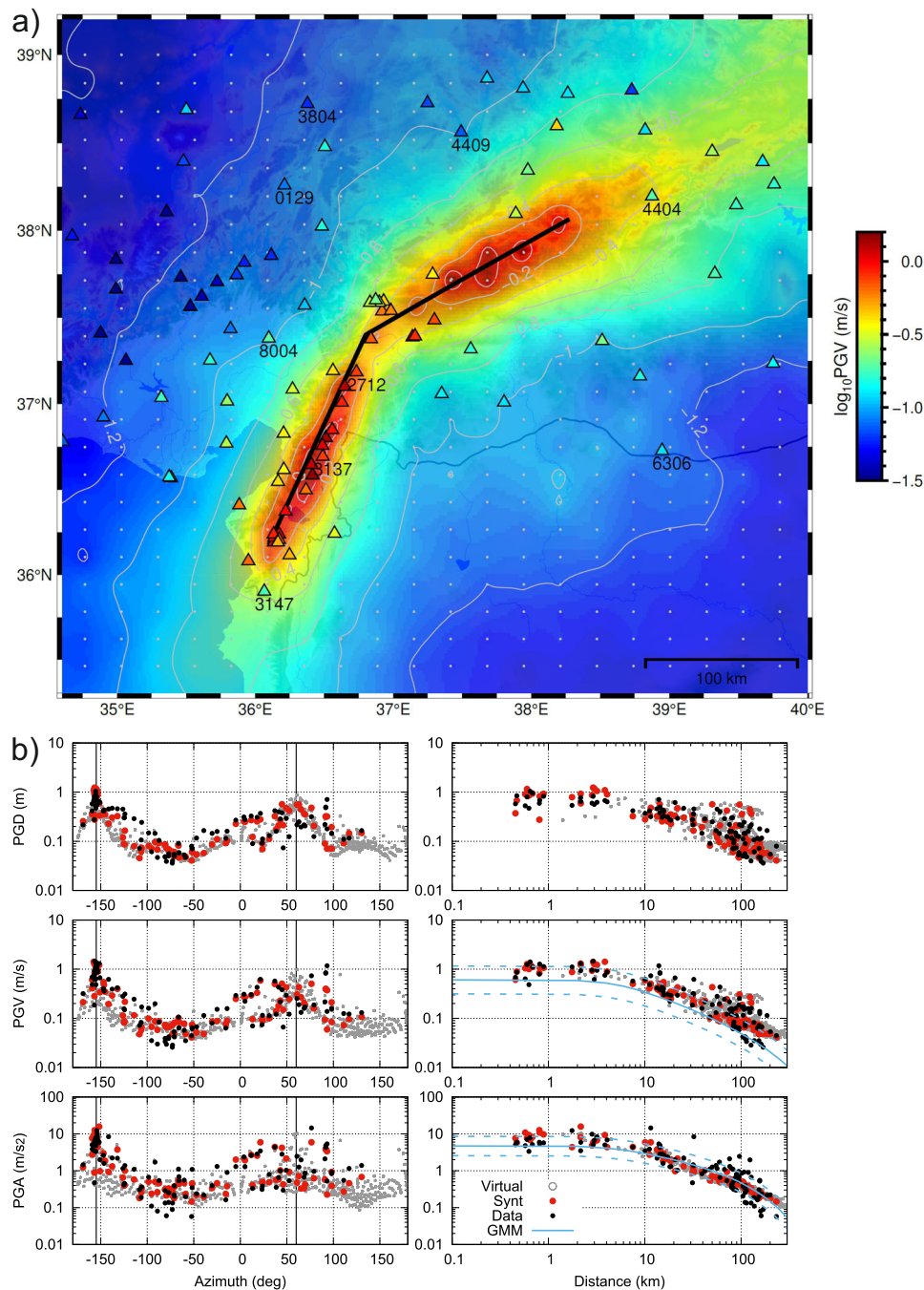


Fig. 4 Comparison of synthetic and observed peak ground motions, assuming rotationally independent mean values (GMRotD50³⁴). **a** Modeled horizontal peak ground velocities (PGV) interpolated from synthetics at virtual stations (gray points) for the preferred broadband model. The trace of the assumed vertical fault is shown by the black line. Real stations are indicated by triangles color-coded by observed PGV; station names are shown only for those with waveforms in Fig. 3a. **b** Peak ground displacements (PGD), velocities (PGV), and accelerations (PGA) from horizontal components as a function of azimuth (left) and distance (right). Black and red dots are observed and synthetic values at the real stations, respectively; gray circles correspond to the virtual stations. Black vertical lines in the left panels indicate the SW and NE azimuths of the fault. The ground motion model (GMM) of PGV and PGA (NGA-West2⁷⁰) is plotted as a blue line in the distance-dependent plots for reference.

Sensitivity tests in Methods demonstrate how various specific source parameters (crossover frequency band in Fig. 5, rupture velocity in Fig. 6a, delay of the SW part of the rupture in Fig. 6b, slip distribution in Fig. 7) are imprinted in the observed recordings. For example, response spectra, commonly used in seismic codes, are affected by the rupture delay very weakly and by the value of constant rupture velocity rather mildly. Also, a generic slip model unconstrained by the GNSS data provides similar response spectra

as the preferred model. The formation of broadband directivity pulses can be captured even with limited knowledge of the rupture velocity once the fault size and rupture direction are known. The present paper thus not only extends so-far published knowledge of the 2023 fault rupture to engineering frequencies, but also serves as a potential sample workflow for rapid physics-based ground-motion estimations for similar future earthquakes that are so far based on interpolation and empirical ground motion models⁴² (ShakeMap).

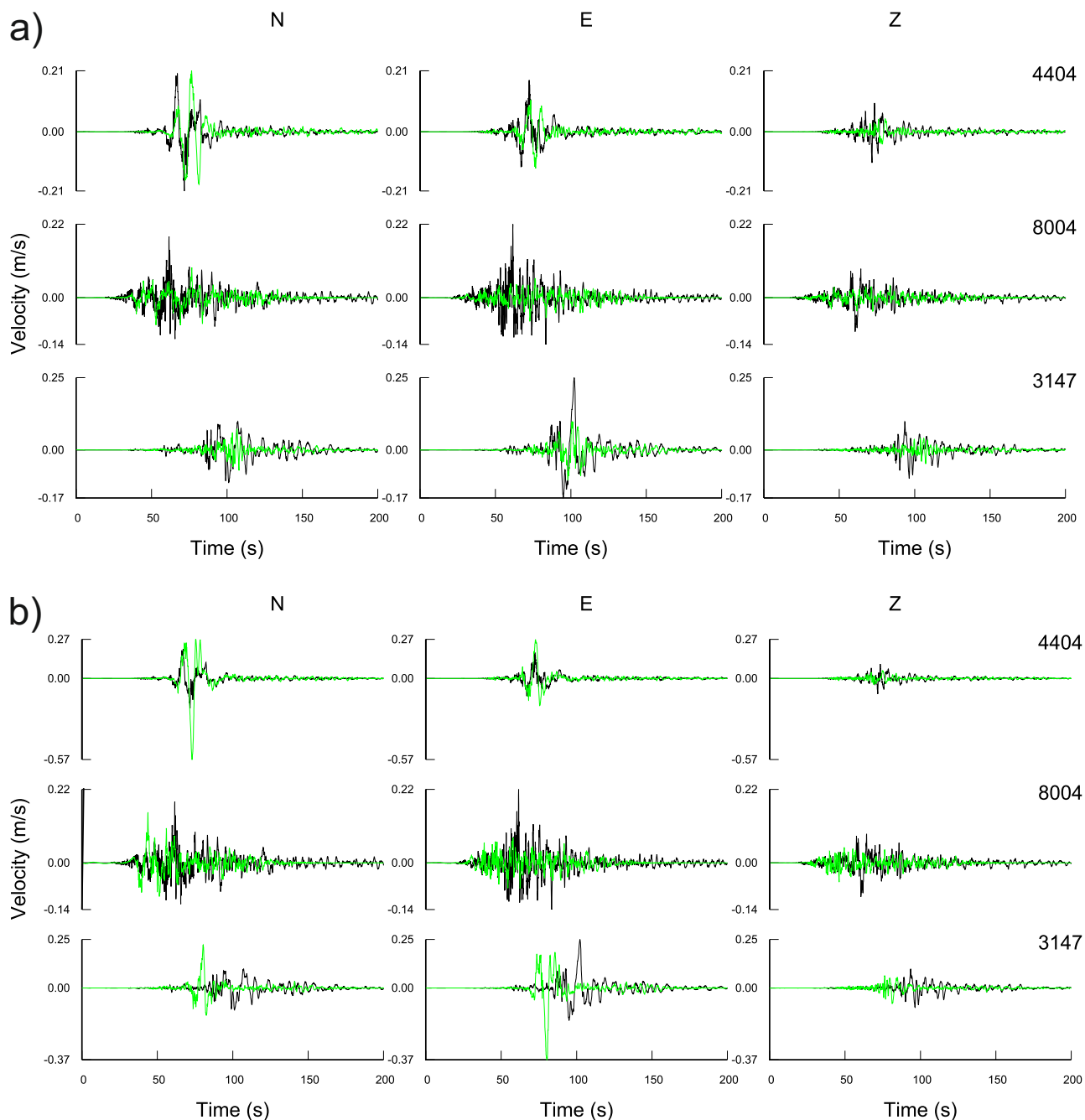


Fig. 5 Effect of the coherent (low-frequency) rupture propagation modeling on the broadband ground motion simulations. **a** Left: Broadband synthetic (green) and observed (black) velocity waveforms for the crossover at higher frequencies (0.25–1.0 Hz) than applied in the preferred model. Right: Spectral acceleration (SA) modeling bias for horizontal components as a function of period (gray lines). Mean and ± 1 standard deviation over stations are shown by green solid and dashed lines, respectively. The red line is the mean SA bias for the preferred model (Fig. 3b) for reference. The test shows the overestimation of the directivity effect due to assuming coherent rupture propagation up to too high frequencies. **b** Same denotation as in panel a, but for omitted coherent part of the simulation, i.e., for a purely incoherent composite model. It demonstrates an underestimation of the directivity effect when the coherent rupture propagation at large scales is omitted.

In seismic hazard assessment, none of the rupture parameters, such as slip distribution, rupture velocity, and location of the nucleation point, can be anticipated for a future event. Therefore, they must be treated as epistemic uncertainty through scenario simulations in physics-based seismic hazard assessment. Our results emphasize the strong ground motion variability due to the source effects, which must be included in such applications. Despite many efforts to have these effects in empirical approaches in a simplified manner^{43,44}, the physics-based modeling

implicitly accounts for them, including their frequency dependence.

Methods

Multiple point-source inversion of seismic data. We use the ISOLA software, which inverts complete seismograms for a multi-point source (MPS) model. ISOLA has been continuously upgraded and applied to reveal earthquake complexities^{25,45–50}. Besides low-parametric character, another advantage is that MPS

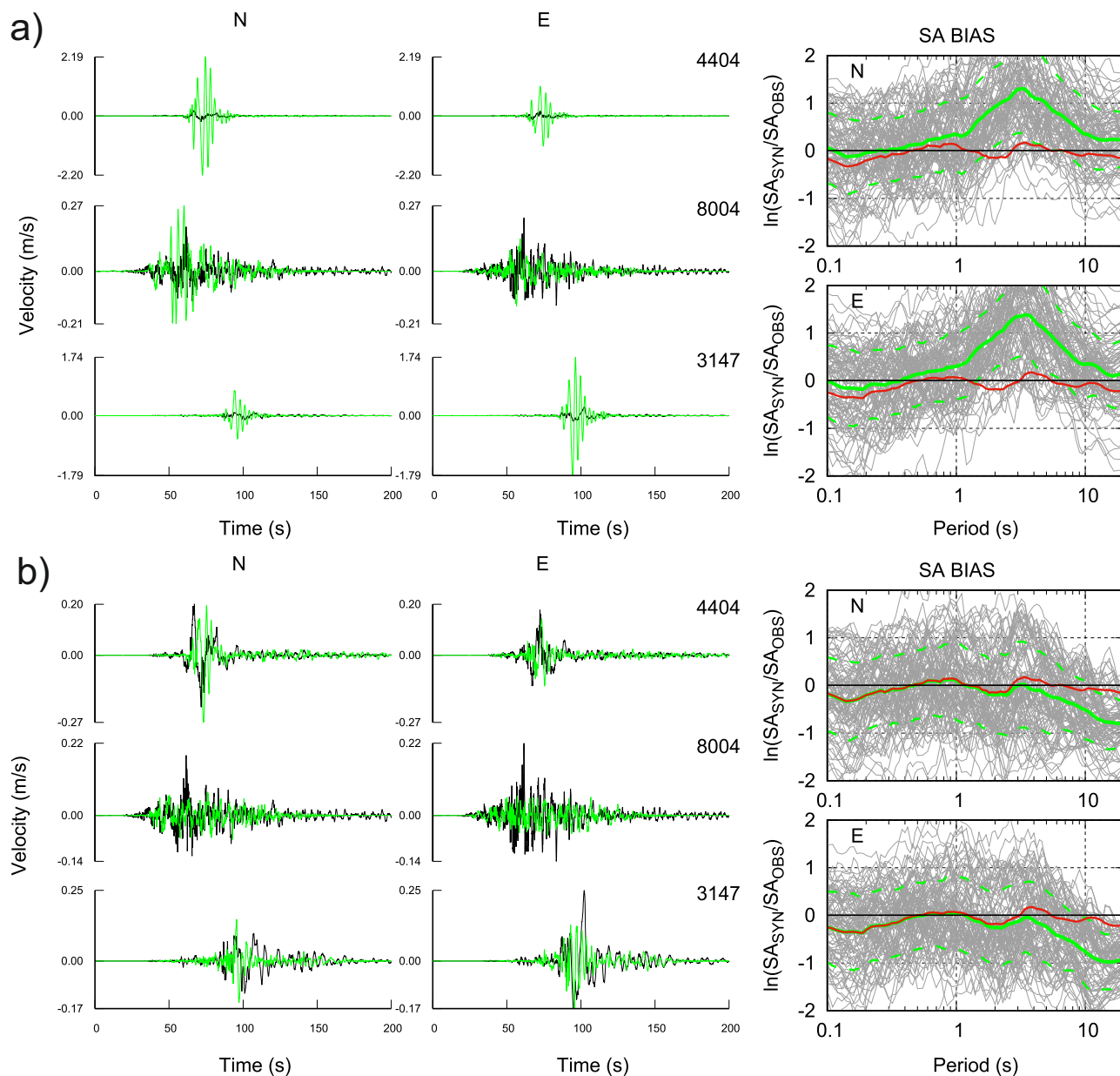


Fig. 6 Effect of rupture velocity and delay of the SW fault segment on broadband synthetic (green) and observed (black) velocity waveforms. **a** When assuming the rupture velocity of 2.5 km/s instead of 3 km/s considered in the preferred model (Test I), the peak values are underestimated, and the directivity pulse is weakened. **b** When neglecting the delay in the SW segment (Test II), the main pulse arrives too early than the observed one at western stations 8004 and 3147. Contrarily, the eastern station 4404 remains unaffected.

solutions are robust to errors in earthquake location and source-geometry specification. It is because subevents are space-time grid-searched in an almost arbitrary set of trial source positions and rupture times. The rupture process is not a priori constrained to start at the hypocenter or to continually proceed along a planar fault segment within prescribed rupture-speed limits.

Even the low-parametric MPS inversions are vulnerable to parameter tradeoffs. Therefore, for example, Duputel and Rivera⁵¹ preferred to fix the spatial positions of the subevents. Analogously, other constraints were discussed by Yue and Lay⁵². Tradeoffs between space-time moment variations and non-double-couple (non-DC) moment tensors might be particularly dangerous. The latter typically accompanies multi-type faulting subevents whose correct structure can only be revealed if seeking 100% DC-constrained subevents⁵³, or prescribing a given focal mechanism.

Several frequency ranges were examined for the 2023 event. Finally, we adopt the minimum inverted frequency of 0.01 Hz to avoid instrumental noise. To avoid errors due to possible inadequacy of the velocity model, we choose the maximum frequency of 0.05 Hz. The same 4th-order causal Butterworth bandpass filter 0.01–0.05 Hz is applied to the real instrumentally corrected seismograms and synthetics, and both are integrated into displacements. We use synthetic full-wavefield Green's functions in the velocity model of Acelar et al.³¹ see section Crustal velocity model. Moment-rate of each subevent is a triangular function of 20-s duration. The fit between real and synthetic bandpass filtered displacement waveforms is quantified with variance reduction, $VR = 1 - |\text{obs} - \text{syn}|^2 / |\text{obs}|^2$, where $|\cdot|$ is the L2 norm. The temporal grid search starts at the origin time (1:17:32 UTC) and ends after 70 seconds. For the preferred mode, the focal mechanism is constrained as follows: strike/dip/

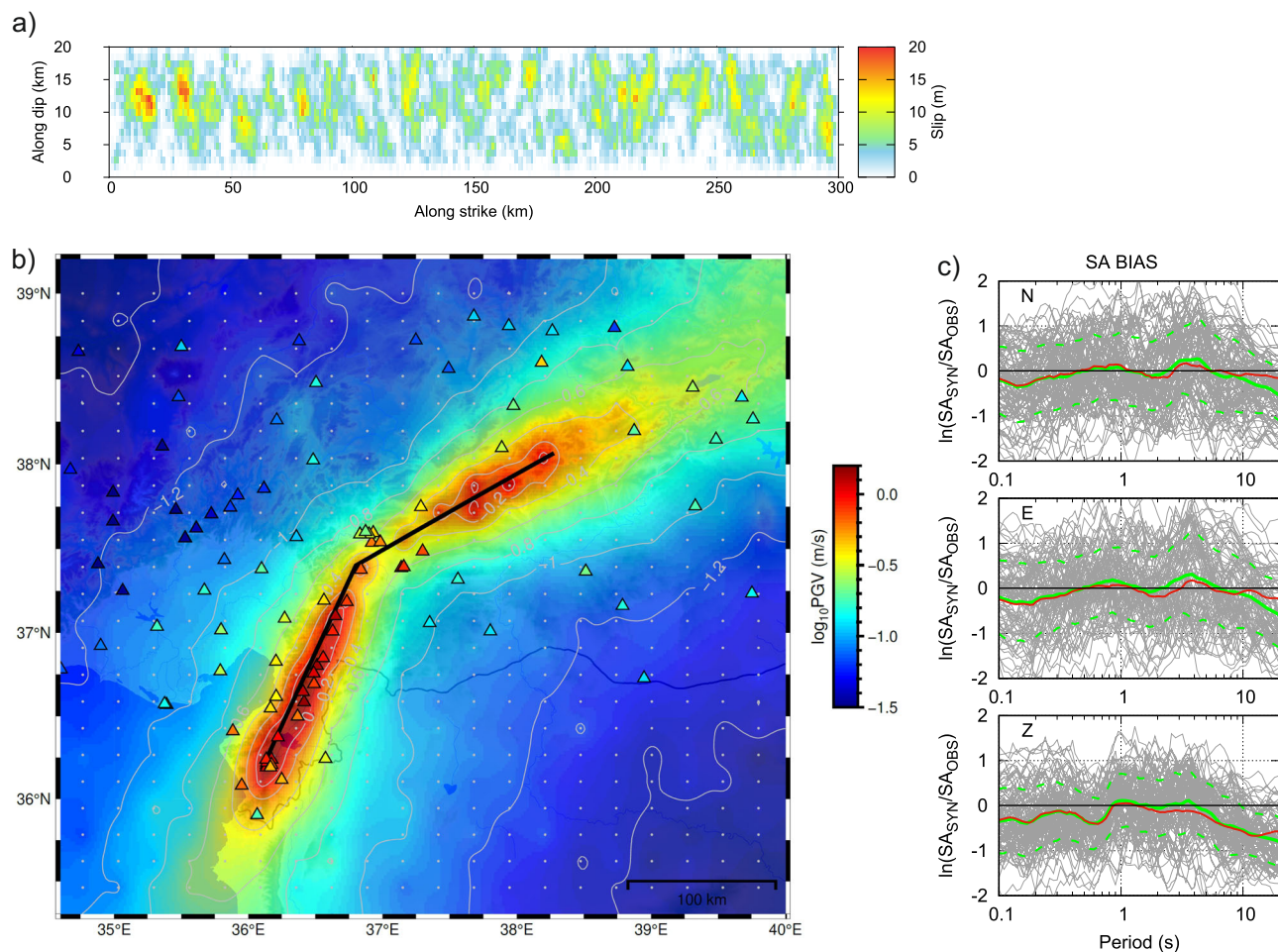


Fig. 7 Effect of slip distribution constraint (Test III). Here we assume a uniform spatial probability density function for the sub-sources instead of constraining them by the GNSS slip inversion. **a** HIC model slip distribution obtained by summing all the sub-source contributions. **b** Horizontal peak ground velocities (GMRotD50 PGV) interpolated from simulated seismograms at virtual stations; compare with Fig. 4a. Black line shows the vertical fault plane. Real stations are shown by triangles color-coded by observed PGV. **c** Modeling spectral acceleration (SA) bias as a function of period (gray lines). Mean and ± 1 standard deviation over stations are shown by green solid and dashed lines, respectively. The red line is the mean SA bias for the preferred model (Fig. 3b) for reference.

rake = $30^\circ/90^\circ/0^\circ$ on the SW segment of EAF and the Narlı splay fault, and $60^\circ/90^\circ/0^\circ$ on the NE segment. The model has variance reduction $VR = 0.70$, and the waveform fit of the 21 strong-motion records is shown in Supplementary Fig. S1.

The stability of the solution is checked by station jackknifing (repeating inversions, each time removing one station); see Supplementary Fig. S2. As the MPS depth resolution was poor, we report stable results at a constant depth of 7.5 km in the Results section. The largest moment release episodes (B and D) on the NE segment of EAF are also the most stable. The least stable is the weak moment release on the Narlı fault. The lower resolution of the SW (F) sub-source can be attributed to the limited southwestward coverage of suitable stations (i.e., located further from the fault). The total seismic moment of this model is 4.0×10^{20} Nm; i.e., moment magnitude $M_w 7.7$ is underestimated by ~ 0.1 due to the absence of frequencies below 0.01 Hz.

Even better data fit ($VR = 0.77$) can be achieved if allowing space variation of the DC-constrained focal mechanism; see Supplementary Fig. S3. It is analogical to allowing varying rake angle in published slip inversions; e.g., Goldberg et al.¹⁰ found an oblique-slip component on EAF near the splay. Normal/reverse faulting components have been geodetically proposed to

supplement major strike-slip faulting on EAF⁵⁴. Non-uniform aftershock mechanisms¹³ indicate that even the mainshock might have included short segments that differ from strike-slip, similar to fault complexity which was indeed identified on the western termination of the second February 6 Mw 7.5 mainshock^{12,15}. Supplementary Fig. S3 demonstrates that MPS with a free DC mechanism confirms the strike-slip faulting on the NE segment, with strike $\sim 60^\circ$ agreeing with fault geometry. However, a possible focal mechanism variation on the SW segment is less clear. As inferred by low solution stability in the jackknife test (Supplementary Fig. S4), we cannot strictly define any stable departure from strike-faulting during mainshock there. Free DC mechanism could also mislocate weak NS episodes around 25 s onto the Narlı fault. Thus, in the preferred model, we use two fixed focal mechanisms.

A preliminary MPS model of 2023 Türkiye mainshocks was released 14 days after the earthquake as an EMSC report, see Data and Resources. We make this note to emphasize the usefulness of the simple MPS method, implying that after data acquisition and quality check, extensive source-inversion testing can be performed shortly after a similar disastrous event. Similarly, the GNSS inversion can be applied quickly once the data and fault geometry are retrieved.

Kinematic slip inversion of GNSS data. We use linear slip inversion of coseismic GNSS displacements to image the slip distribution using open-source code LinSlipInv²⁸. We assume a planar fault with a kink. Synthetic displacements are calculated according to Okada⁵⁵. The inversion is stabilized by the positivity constraint⁵⁶ and by prescribing an isotropic correlation function of model parameters with k^{-2} amplitude spectrum (where k is the radial wavenumber), which smooths the slip distribution. The smoothing strength is controlled by a non-dimensional ratio between the standard deviations of the model parameters and data (further called the relative smoothing weight). The optimal smoothing is found by a grid search based on the resulting data misfit and inferred seismic moment.

We test the strength of the smoothing through varying relative smoothing weight s_w in a sufficiently wide range to observe the sensitivity of the inversion. Supplementary Fig. S5 demonstrates that the GNSS data are almost equally well-fitted for any $s_w \leq 2$. Moment decreases below 4.5×10^{20} Nm for $s_w < 0.8$ and $s_w > 8.0$. The moment peaks for $s_w = 2$ at $M_0 = 4.8 \times 10^{20}$ Nm with $VR = 0.61$, see Fig. 2. For examples of stronger and weaker smoothing models, see Supplementary Fig. S5. We note that the data fit at the EKZ1 station can be improved by allowing a spatially varying strike and dip with only a minor effect on the slip distribution¹². Nevertheless, here we prefer a simpler and more robust model of Fig. 2.

The dependence of the inverted slip models on the smoothing strength allows for a rough estimate of the inversion resolution. Indeed, the weaker the smoothing is, the more concentrated the slip patches are (Supplementary Fig. S2). The minimum patch size for the preferred smoothing level suggests a lateral resolution of about ~ 50 km. The depth resolution is lower than the width of the fault due to the vertical geometry and the use of surface stations.

Broadband hybrid integral-composite source model. For the broadband ground motion simulations, we use the Hybrid Integral-Composite (HIC) technique by Gallovič and Brokešová³⁰, which was previously applied to modeling of, e.g., the 2009 Mw 6.2 L'Aquila (Central Italy⁵⁷) or the 2011 Mw 7.1 Van (Eastern Turkey⁵⁸) earthquakes. It represents the rupture process by overlapping rectangular subsources with random slip distribution having k^{-2} decay at high wavenumbers k . The subsources are randomly distributed on the fault with fractal number-size distribution; the number of subsources increases linearly with decreasing subsource size. The subsources are characterized by a constant stress-drop scaling, composing a slip distribution on the whole fault with k^{-2} decay. We constrain the random spatial distribution of the subsources (independently of their size) by prescribing a probability density function (PDF) over the fault. It is considered equal to the slip distribution from the GNSS inversion (Fig. 2b) plus a water level of 10% of the slip maximum; further, the PDF is normalized to a unit integral. Thus, the subsources tend to localize in the asperity areas, but not exclusively there due to the water level (compare Figs. 2c and 7a for the constrained and unconstrained case).

The subsources are treated differently in the low- and high-frequency ranges. As described below, the two procedures result in seismograms, which are then combined in a crossover frequency interval (f_1, f_2) by weighted averaging of the real and imaginary parts of their Fourier spectra using \cos^2 and \sin^2 functions. The two approaches are as follows (see Gallovič and Brokešová³⁰, for more details).

Up to frequency f_2 , the integral of the representation theorem⁵⁹ is evaluated: The fault is discretized into a regular grid of subsources. At each subfault, the slip is computed as a sum of

contributions from all subsources covering the subfault. The rupture time is calculated from the distance of the subfault to the nucleation point of the earthquake and the prescribed (constant) rupture velocity v_r . The slip velocity function has Brune pulse shape with a constant rise time of 0.1 s. We note that it is shorter than the reciprocal of f_2 and thus does not affect the synthetics. Green's functions (GFs) are calculated from the center of each subfault, and the synthetics are obtained by convolving slip rates with the GFs and integrating over the fault. In this approach, the directivity of the rupture propagation is well captured at low frequencies due to the coherent summation of the subfaults' wavefield contributions.

Above f_1 , the composite approach is used: The individual subsources are treated as point sources with Brune source time function, described by their respective seismic moments and corner frequencies (assuming a constant stress drop scaling). Synthetics for a given subsource are obtained by convolution of the source time functions (Brune pulse) with GFs calculated from the subsource's center. These contributions are then shifted by their respective rupture time, calculated as the time that the rupture needs to reach the center of the subsource, considering the same rupture velocity v_r as in the integral approach, and summed. In contrast to the integral part, the directivity effect is suppressed due to the incoherent summation of the subsources' wavefield contributions. We add random variations in strike, dip, and rake to the mechanisms of the subsources to weaken the effect of the radiation pattern at high frequencies, in agreement with empirical studies^{60,61}.

The seismic moments of the subsources m_{0i} are constrained so that their sum gives the earthquake's total scalar seismic moment M_0 . In the composite approach, the subevents' corner frequencies are adjusted so that the resulting high-frequency acceleration plateau of the event has a prescribed height. For the Brune omega-square source time function, the height of the acceleration spectral plateau is equal to $A = M_0 f_c^2$ with f_c being the event corner frequency, respectively. We assume that f_c is related to the stress drop of a crack model⁶²⁻⁶⁵,

$$\Delta\sigma = \frac{7}{16} \left(\frac{f_c}{kv_s} \right)^3 M_0 \quad (2)$$

where v_s is the shear-wave velocity, and k is a parameter depending on the details of the rupture model (e.g., heterogeneity of slip and rupture velocity). Since $\Delta\sigma$ is treated rather formally in the HIC model, we refer to it as the stress parameter and consider $k = 0.37$ ⁶². We consider the corner frequency of the subsources as $\hat{f}_{ci} = \frac{av_r}{l_i}$, where l_i is the subsource length, and a is an unknown parameter. Assuming incoherent summation of the subsources' contributions at high frequencies, the total height of the earthquake spectral plateau squared is,

$$A^2 = \sum_i m_{0i}^2 \hat{f}_{ci}^4 \quad (3)$$

For prescribed M_0 and $\Delta\sigma$, parameter a can then be determined from Eqs. (2) and (3).

To summarize, the HIC model parameters for fixed M_0 , fault area, and nucleation point are: i) the layout of subsources (and thus the resulting slip distribution), ii) rupture velocity v_r , and iii) stress parameter $\Delta\sigma$. We point out that it is straightforward to introduce specific time delays in the rupture propagation, as needed here, by increasing the rupture times of the subfaults and subsources. The parameters are constrained based on preliminary geodetic and low-frequency seismic data inversions and by trial-and-error comparisons of the broadband simulations with the recordings in both time and frequency domains.

Following Ameri et al.⁵⁷, we assume two crossover frequency ranges depending on the station distance from the rupture. While we consider 0.1–0.4 Hz for stations within 10 km from the fault, we use 0.05–0.2 Hz elsewhere. We perform two tests to demonstrate the adequacy of the considered crossover frequency ranges and facilitate discussion regarding their significance. Firstly, we test the crossover at higher frequencies (0.25–1.0 Hz), i.e., applying the coherent integral technique to higher frequencies. Figure 5a shows the corresponding velocity waveforms for the selected stations and the SA bias for all stations, including its mean and variability. The SA bias shows systematic overestimation in the 2–10 s period range. The waveform comparison then demonstrates that it is due to unrealistically strong directivity amplification in the integral (coherent) part of the synthetics. Secondly, assuming only the composite model (i.e., omitting the integral approach in the low-frequency band) leads to substantial underestimation at periods larger than ~5 s, see Fig. 5b. This is due to the incoherent summation of the wavefield contributions of the subsources that reduce the directivity effect, contradicting the observations. Indeed, this is expressed by the inhibited velocity pulses in the synthetics at all selected stations shown in Fig. 5b.

We point out that the preferred frequency ranges are smaller than ~1 Hz, typically assumed in broadband simulation methods that combine the deterministic calculations at low frequencies with stochastic approaches at high frequencies⁶⁶. Ameri et al.⁵⁷ used considerably higher crossover frequency ranges (1.5–2 Hz for near-field and 0.15–0.6 Hz for far-field stations) in their modeling of the Mw6.3 L'Aquila earthquake, perhaps due to the smaller magnitude of the studied event. The loss of coherency needed even for the very near-fault stations suggests complexity in the rupture propagation at short scales. In dynamic rupture modeling, such an effect can be attained by considering small-scale random variability of rupture geometry³⁸ and/or random perturbations of the fracture energy and initial stress³⁹. Nevertheless, the composite model is an efficient, practical approach that approximates such strong heterogeneity of the rupture propagation at short scales by the incoherent summations of the wavefield contribution from subsources treated as point sources.

Crustal velocity model. Both ISOLA and HIC use code Axitra⁶⁷ based on the discrete wavenumber method⁶⁸ to calculate synthetic full-wavefield Green's functions in the full frequency range in a 1D layered medium. For the low-frequency inversion by ISOLA, we employ the 1D velocity model of Acarel et al.³¹, see Supplementary Table S2. The model has a 2-km thick subsurface layer with S-wave velocity V_s of 2.78 km/s, which is adequate for low-frequency modeling but does not sufficiently describe site effects. For the broadband modeling, we have thus added 5 shallow layers to approximate a generic rock site with 800 m/s subsurface V_{s30} S-wave velocity, see Supplementary Table S3. Supplementary Fig. S6 shows how adding these layers corrects the systematic frequency dependent-underestimation of synthetics present in the spectral bias plot with the original velocity model.

Sensitivity of the broadband model

Lower rupture velocity (Test I). Figure 6a illustrates the effect of assuming a lower rupture velocity $v_r = 2.5$ km/s on velocity waveforms for three selected stations, namely 8004, lying west of the fault kink, and stations 4404 and 3147 located at the NE and SW terminations of the rupture, respectively. The directivity pulses are less well-fitted at the three stations. In particular, at NE station 4404, the single pulse at the north component splits in two with smaller amplitudes, unlike in the observations. Similar

effects can be seen on the east component of station 3147 lying in SW. We point out that the described effects are consonantly affecting other stations in similar directions.

No rupture delay in the SW segment (Test II). If the 15-s rupture delay of the SW segment is not considered, the directivity pulses of the velocity synthetics in the SW stations arrive systematically too early. It is visible in Fig. 6b for station 3147 lying close to the SW termination of the rupture. Contrarily, stations lying to NE, such as 4404 in Fig. 6b, remain unaffected as the wavefield contribution from the opposite side of the fault is minor, due to the geometrical distance. Station 8004, located west of the NE part of the fault, but north of the SW segment, also exhibits poor timing of the synthetic initial directivity pulse, suggesting that the rupture was delayed already at the intersection (junction) between EAF and the NNE-striking Narlı splay fault, not at the fault kink. Note that the physical mechanism for the time delay of the rupture backpropagating along EAF from the junction towards SW was also independently proposed by Abdelmeguid et al.¹⁹ and Jia et al.²¹. Indeed, their dynamic simulation shows that the SW rupture propagation along EAF became mechanically viable only after enough stress drop (and thus slip) occurred along the NE part of EAF.

Uniform distribution of subsources (Test III). We test a generic model unconstrained by the GNSS data. Here we assume a uniform spatial PDF for the distribution of the subsources; see an example in Fig. 7a. The slip distribution is still heterogeneous but does not concentrate in asperities as in Fig. 2c. All other parameters, including the time delay of the SW fault branch, remain the same. Figure 7b shows the resulting PGV map. Both the constrained (Fig. 4a) and unconstrained PGV maps are similar along the SW branch of the rupture, while the PGV values are smaller for the unconstrained model of Fig. 7b along the NE segment, especially in the epicentral area. The latter is because the near-fault PGVs are dictated by the directivity pulse that develops only after the rupture passes a sufficient distance. Nevertheless, as confirmed by the SA bias in Fig. 7c, the fit is like that of the preferred model. This test suggests that the details of the slip distribution are less important than other source parameters, even at near-fault regions.

Data availability

Strong motion data used in this study were produced by the Disaster and Emergency Management Authority of Türkiye (AFAD – TK), <https://tdvms.afad.gov.tr>. We used GNSS data of Event 1 from Taymaz et al., available at https://www.emsc-csem.org/Files/event/1218444/M7.8_updated_text_13-2-2023.pdf (last accessed February 27, 2023), provided by CORS-TR (TUSAGA-Aktif-Türkiye) administered by General Directorate of Land Registry and Cadastre (TKGM) and General Directorate of Mapping (HGM). We thank all the staff involved in building and running high-quality Turkish networks. A preliminary MPS model of both 2023 Türkiye earthquakes was submitted as a report to EMSC (https://static3.emsc.eu/Doc/Additional_Earthquake_Report/1218444/Report_EMSC.pdf). The study is based on synthetic calculations; processed data and synthetics from broadband simulations are available from the Zenodo data repository (<https://doi.org/10.5281/zenodo.8414742>).

Code availability

Code DC3D (Okada, 1992) is available at <https://www.bosai.go.jp/edc3d.html>. Continuous static GNSS inversion was performed using LinSlipInv (<http://fgallovic.github.io/LinSlipInv/>). The ISOLA software²⁵ used in this paper can be downloaded from https://geo.mff.cuni.cz/~jz/for_ISOLANews/ and <https://github.com/esokos/isola>. The maps were generated using the Generic Mapping Tools v6⁶⁹.

Received: 22 June 2023; Accepted: 27 October 2023;

Published online: 11 November 2023

References

- Duman, T. Y. & Emre, Ö. *The East Anatolian Fault: geometry, segmentation and jog characteristics*, (Geological Development of Anatolia and the Easternmost Mediterranean Region, 2013).
- Karabulut, H., Güvercin, S. E., Hollingsworth, J. & Konca, A. Ö. Long silence on the East Anatolian Fault Zone (Southern Turkey) ends with devastating double earthquakes (6 February 2023) over a seismic gap: implications for the seismic potential in the Eastern Mediterranean region. *J. Geol. Soc.* **180**, jgs2023–021 (2023).
- Hall, S. What Turkey's earthquake tells us about the science of seismic forecasting. *Nature* **615**, 388–389 (2023).
- Dal Zilio, L. & Ampuero, J.-P. Earthquake doublet in Turkey and Syria. *Commun. Earth Environ.* **4**, 71 (2023).
- Gürer, D., Hubbard, J. & Bohon, W. Science on social media. *Commun. Earth Environ.* **4**, 148 (2023).
- Lekkas, E. et al. *The 6 February 6 2023 Turkey-Syria Earthquakes* (Newsletter of Environmental, Disaster and Crises Management Strategies, 2023) 29, ISSN 2653-ISSN 9454.
- Hancılar, U. et al. *Kahramanmaraş – Gaziantep Türkiye M7.7 Earthquake, 6 February 2023 (04:17 GMT+03:00): strong ground motion and building damage estimations preliminary report (v6)* (Boğaziçi University, Kandilli Observatory and Earthquake Research Institute, Department of Earthquake Engineering, 2023).
- Cetin, K. & Ilgac, M. Reconnaissance Report on February 6, 2023 Kahramanmaraş-Pazarcık (Mw=7.7) and Elbistan (Mw=7.6) Earthquakes. *Türkiye Earthq. Reconnaiss. Res. Alliance*. <https://doi.org/10.13140/RG.2.2.15569.61283/1> (2023).
- Karabacak, V. et al. The 2023 Pazarcık (Kahramanmaraş, Türkiye) earthquake (Mw 7.7): implications for surface rupture dynamics along the East Anatolian Fault Zone. *J. Geol. Soc.* **180**, jgs2023–020 (2023).
- Goldberg, D. E. et al. Rapid characterization of the February 2023 Kahramanmaraş, Türkiye, earthquake sequence. *Seismic Record* **3**, 156–167 (2023).
- Mai, P. M. et al. The destructive earthquake doublet of 6 February 2023 in South-Central Türkiye and Northwestern Syria: initial observations and analyses. *Seismic Record* **3**, 105–115 (2023).
- Zahradník, J., Turhan, F., Sokos, E. & Gallovič, F. Asperity-like (segmented) structure of the 6 February 2023 Turkish earthquakes. *EarthArXiv*. <https://doi.org/10.31223/X5T666> (2023).
- Petersen, G. M. et al. The 2023 Southeast Türkiye seismic sequence: rupture of a complex fault network. *Seismic Record* **3**, 134–143 (2023).
- Melgar, D. et al. Sub- and super-shear ruptures during the 2023 Mw 7.8 and Mw 7.6 earthquake doublet in SE Türkiye. *Seismica* **2**, 3 (2023).
- Okuwaki, R., Yagi, Y., Taymaz, T. & Hicks, S. P. Multi-scale rupture growth with alternating directions in a complex fault network during the 2023 south-eastern Türkiye and Syria earthquake doublet. *Geophys. Res. Lett.* **50**, e2023GL103480 (2023).
- Taymaz, T. et al. Source mechanism and rupture process of the 24 January 2020 Mw 6.7 Doğanyol-Sivrice earthquake obtained from seismological waveform analysis and space geodetic observations on the East Anatolian Fault Zone (Turkey). *Tectonophysics* **804**, 228745 (2021).
- Gallovič, F. et al. Complex rupture dynamics on an immature fault during the 2020 Mw 6.8 Elazığ earthquake, Turkey. *Commun. Earth Environ.* **1**, 40 (2020).
- Rosakis, A., Abdelmeguid, M. & Elbanna, A. Evidence of early supershear transition in the Mw 7.8 Kahramanmaraş earthquake from near-field records, pre-print. *EarthArXiv* <https://doi.org/10.31223/X5W95G> (2023).
- Abdelmeguid, M. et al. Revealing the dynamics of the Feb 6th 2023 M7.8 Kahramanmaraş/Pazarcık Earthquake: near-field records and dynamic rupture modeling. Preprint at <https://doi.org/10.48550/arXiv.2305.01825> (2023).
- Wang, Z. et al. Dynamic rupture process of the 2023 Mw 7.8 Kahramanmaraş earthquake (SE Türkiye): Variable rupture speed and implications for seismic hazard. *Geophys. Res. Lett.* **50**, e2023GL104787 (2023).
- Jia, Z. et al. The complex dynamics of the 2023 Kahramanmaraş, Turkey, Mw 7.8–7.7 earthquake doublet. *Science* **381**, 985–990 (2023).
- Wu, F. et al. Pulse-like ground motion observed during the 6 February 2023 MW7.8 Pazarcık Earthquake (Kahramanmaraş, SE Türkiye). *Earthq. Sci.* **36**, 328–339 (2023).
- Hall, J. F., Heaton, T. H., Halling, M. W. & Wald, D. J. Near-source ground motion and its effects on flexible buildings. *Earthq. Spectra* **11**, 569–605 (1995).
- Champion, C. & Liel, A. The effect of near-fault directivity on building seismic collapse risk. *Earthq. Eng. Struct. Dyn.* **41**, 1391–1409 (2012).
- Zahradník, J. & E. Sokos ISOLA code for multiple-point source modeling—Review, in *Moment Tensor Solutions: A Useful Tool for Seismotectonics*, S. D'Amico (Editor), Springer International Publishing, Cham, Switzerland, 1–28 (2018).
- Reitman, N. G. et al. *Fault rupture mapping of the 6 February 2023 Kahramanmaraş, Türkiye, earthquake sequence from satellite data: U.S. Geological Survey data release* <https://doi.org/10.5066/P985I7U2> (2023).
- Kikuchi, M. & Kanamori, H. Inversion of complex body waves. III. *Bull. Seism. Soc. Am.* **81**, 2335–2350 (1991).
- Gallovič, F., Imperatori, W. & Mai, P. M. Effects of three-dimensional crustal structure and smoothing constraint on earthquake slip inversions: case study of the Mw6.3 2009 L'Aquila earthquake. *J. Geophys. Res.* **120**, 428–449 (2015).
- Ozer, C., Ozyaziciglu, M., Gök, E. & Polat, O. Imaging the crustal structure throughout the East Anatolian Fault Zone, Turkey, by Local Earthquake Tomography. *Pure Appl. Geophys.* **176**, 2235–2261 (2019).
- Gallovič, F. & Brokešová, J. Hybrid k-squared source model for strong ground motion simulations: introduction. *Phys. Earth Planet. Inter.* **160**, 34–50 (2007).
- Acarel, D., Cambaz, M. D., Turhan, F., Mutlu, A. K. & Polat, R. Seismotectonics of Malatya fault, Eastern Turkey. *Open Geosci.* **11**, 1098–1111 (2019).
- Pitarka, A. et al. Refinements to the Graves–Pitarka kinematic rupture generator, including a dynamically consistent slip-rate function, applied to the 2019 Mw 7.1 Ridgecrest. *Bull. Seismol. Soc. Am.* **112**, 287–306 (2021).
- Baltzopoulos, G. et al. Near-source ground motion in the M7. 8 Gaziantep (Turkey) earthquake. *Earthq. Eng. Struct. Dyn.* **52**, 3903–3912 (2023).
- Boore, D. M. Orientation-independent, nongeometric-mean measures of seismic intensity from two horizontal components of motion. *Bull. Seismol. Soc. Am.* **100**, 1830–1835 (2010).
- Ameri, G., Emolo, A., Pacor, F. & Gallovič, F. Ground-motion simulations for the 1980 M 6.9 Irpinia earthquake (southern Italy) and scenario events. *Bull. Seismol. Soc. Am.* **101**, 1136–1151 (2011).
- Pacor, F., Gallovič, F., Puglia, R., Luzi, L. & D'Amico, M. Diminishing high-frequency directivity due to a source effect: Empirical evidence from small earthquakes in the Abruzzo region, Italy. *Geophys. Res. Lett.* **43**, 5000–5008 (2016).
- Colavitti, L., Lanzano, G., Sgobba, S., Pacor, F. & Gallovič, F. Empirical evidence of frequency-dependent directivity effects from small-to-moderate normal fault earthquakes in central Italy. *J. Geophys. Res. Solid Earth* **127**, e2021JB023498 (2022).
- Taufiqurrahman, T., Gabriel, A.-A., Ulrich, T., Valentová, L. & Gallovič, F. Broadband dynamic rupture modeling with fractal fault roughness, frictional heterogeneity, viscoelasticity and topography: the 2016 Mw 6.2 Amatrice, Italy earthquake. *Geophys. Res. Lett.* **49**, e2022GL098872 (2022).
- Gallovič, F. & Valentová, L. Broadband strong ground motion modeling using planar dynamic rupture with fractal parameters. *J. Geophys. Res.* **128**, e2023JB026506 (2023).
- Kaneko, Y., Lapusta, N. & Ampuero, J.-P. Spectral element modeling of spontaneous earthquake rupture on rate and state faults: Effect of velocity-strengthening friction at shallow depths. *J. Geophys. Res.* **113**, B09317 (2008).
- Jiang, J., Bock, Y. & Klein, E. Coevolving early afterslip and aftershock signatures of a San Andreas fault rupture. *Sci. Adv.* **7**, eabc1606 (2021).
- Worden, C. B. et al. Spatial and spectral interpolation of ground-motion intensity measure observations. *Bull. Seism. Soc. Am.* **108**, 866–875 (2018).
- Spudich, P., Rowshandel, B., Shahi, S. K., Baker, J. W. & Chiou, B. S.-J. Comparison of NGA-West2 directivity models. *Earthq. Spectra* **30**, 1199–1221 (2014).
- Spagnuolo, E., Akinci, A., Herrero, A. & Pucci, S. Implementing the effect of the rupture directivity on PSHA for the City of Istanbul, Turkey. *Bull. Seism. Soc. Am.* **106**, 2599–2613 (2016).
- Sokos, E. & Zahradník, J. Evaluating centroid-moment-tensor uncertainty in the new version of ISOLA software. *Seismol. Res. Lett.* **84**, 656–665 (2013).
- Sokos, E. et al. Asperity break after 12 years: The Mw6.4 2015 Lefkada (Greece) earthquake. *Geophys. Res. Lett.* **43**, 6137–6145 (2016).
- Liu, J. et al. North Korea's 2017 test and its nontectonic aftershock. *Geophys. Res. Lett.* **45**, 3017–3025 (2018).
- Liu, J. & Zahradník, J. The 2019 MW 5.7 Changning earthquake, Sichuan Basin, China: a shallow doublet with different faulting styles. *Geophys. Res. Lett.* **47**, e2019GL085408 (2020).
- Hicks, S. P. et al. Back-propagating supershear rupture in the 2016 Mw 7.1 Romanche transform fault earthquake. *Nat. Geosci.* **13**, 647–653 (2020).
- Turhan, F. et al. Coseismic faulting complexity of the 2019 Mw 5.7 Silivri earthquake in the Central Marmara Seismic Gap, offshore Istanbul. *Seismol. Res. Lett.* **94**, 75–86 (2023).
- Duputel, Z. & Rivera, L. Long-period analysis of the 2016 Kaikoura earthquake. *Phys. Earth Planet. Inter.* **265**, 62–66 (2017).
- Yue, H. & Lay, T. Resolving complicated faulting process using Multi-Point-Source representation: Iterative inversion algorithm improvement and application to recent complex earthquakes. *J. Geophys. Res. Solid Earth* **125**, e2019JB018601 (2020).
- Sokos, E. et al. The 2018 Mw 6.8 Zakynthos, Greece, earthquake: dominant strike-slip faulting near subducting slab. *Seismol. Res. Lett.* **91**, 721–732 (2020).

54. Özkan, A., Yavaşoğlu, H. H. & Masson, F. Present-day strain accumulations and fault kinematics at the Hatay Triple Junction using new geodetic constraints. *Tectonophysics* **854**, 229819 (2023).
55. Okada, Y. Internal deformation due to shear and tensile faults in a half-space. *Bull. Seismol. Soc. Am.* **82**, 1018–1040 (1992).
56. Lawson, C. L., & R. J. Hanson Solving least squares problems. In *Prentice-Hall Series in Automatic Computation*, 340, (Prentice-Hall, Upper Saddle River, N. J, 1974).
57. Ameri, G., Gallovič, F. & Pacor, F. Complexity of the Mw6.3 2009 L'Aquila (Central Italy) earthquake: 2. Broadband strong-motion modeling. *J. Geophys. Res.* **117**, B04308 (2012).
58. Gallovič, F. et al. Fault process and broadband ground-motion simulations of the 23 October 2011 Van (Eastern Turkey) earthquake. *Bull. Seismol. Soc. Am.* **103**, 3164–3178 (2013).
59. Aki, K. & P. G. Richards *quantitative seismology*. 2nd ed., 700 (CA: University Science Books, Sausalito, 2002).
60. Kotha, S. R., Cotton, F. & Bindi, D. Empirical models of shear-wave radiation pattern derived from large datasets of ground-shaking observations. *Sci. Rep.* **9**, 981 (2019).
61. Trugman, D. T., Chu, S. X. & Tsai, V. C. Earthquake source complexity controls the frequency dependence of near-source radiation patterns. *Geophys. Res. Lett.* **48**, e2021GL095022 (2021).
62. Brune, J. N. Tectonic stress and the spectra of seismic shear waves from earthquakes. *J. Geophys. Res.* **75**, 4997–5009 (1970).
63. Kaneko, Y. & Shearer, P. M. Variability of seismic source spectra, estimated stress drop, and radiated energy, derived from cohesive-zone models of symmetrical and asymmetrical circular and elliptical ruptures. *J. Geophys. Res. Solid Earth* **120**, 1053–1079 (2015).
64. Wang, Y. & Day, S. M. Seismic source spectral properties of crack-like and pulse-like modes of dynamic rupture. *J. Geophys. Res. Solid Earth* **122**, 6657–6684 (2017).
65. Gallovič, F. & Valentová, L. Earthquake stress drops from dynamic rupture simulations constrained by observed ground motions. *Geophys. Res. Lett.* **47**, e2019GL085880 (2020).
66. Graves, R. W. & Pitarka, A. Broadband ground-motion simulation using a hybrid approach. *Bull. Seismol. Soc. Am.* **100**, 2095–2123 (2010).
67. Cotton, F. & Coutant, O. Dynamic stress variations due to shear faults in a plane-layered medium. *Geophys. J. Int.* **128**, 676–688 (1997). 3.
68. Bouchon, M. A simple method to calculate Green's functions for elastic layered media. *Bull. Seism. Soc. Am.* **71**, 959–971 (1981).
69. Wessel, P. et al. The Generic Mapping Tools version 6. *Geochemistry, Geophysics, Geosystems* **20**, 5556–5564 (2019).
70. Boore, D. M., Stewart, J. P., Seyhan, E. & Atkinson, G. M. NGAWest2 equations for predicting PGA, PGV, and 5% damped PSA for shallow crustal earthquakes. *Earthq. Spectra* **30**, 1057–1085 (2014).

Acknowledgements

We thank the Czech Science Foundation (grant 23-06345S) and Charles University (grant SVV 260709) for the financial support.

Author contributions

F.C. conducted the kinematic finite fault modeling, J.Z., E.S. and F.T. performed the multiple point source inversions, F.T. provided expertise on the East Anatolian Fault and data, F.G. carried out the static slip inversion from GNSS data. All authors contributed to writing the manuscript.

Competing interests

The authors declare no competing interests.

Additional information

Supplementary information The online version contains supplementary material available at <https://doi.org/10.1038/s43247-023-01076-x>.

Correspondence and requests for materials should be addressed to František Čejka.

Peer review information *Communications Earth & Environment* thanks the anonymous reviewers for their contribution to the peer review of this work. Primary Handling Editors: Luca Dal Zilio and Joe Aslin. A peer review file is available.

Reprints and permission information is available at <http://www.nature.com/reprints>

Publisher's note Springer Nature remains neutral with regard to jurisdictional claims in published maps and institutional affiliations.



Open Access This article is licensed under a Creative Commons

Attribution 4.0 International License, which permits use, sharing, adaptation, distribution and reproduction in any medium or format, as long as you give appropriate credit to the original author(s) and the source, provide a link to the Creative Commons licence, and indicate if changes were made. The images or other third party material in this article are included in the article's Creative Commons licence, unless indicated otherwise in a credit line to the material. If material is not included in the article's Creative Commons licence and your intended use is not permitted by statutory regulation or exceeds the permitted use, you will need to obtain permission directly from the copyright holder. To view a copy of this licence, visit <http://creativecommons.org/licenses/by/4.0/>.

© The Author(s) 2023